Citizen scientists report global rapid reductions in the visibility of stars from 2011 to 2022

Christopher C.M. Kyba,[1,2*] Yiğit Öner Altıntaş,[1,†] Constance E. Walker,[3] Mark Newhouse[4]

[1]Remote Sensing and Geoinformatics, Deutsches GeoForschungsZentrum Potsdam, Potsdam 14473, Germany

[2]Geographisches Institut, Ruhr-Universität Bochum, Bochum 44780, Germany

[3]Office of Observatory Site Protection, National Optical-Infrared Astronomy Research Laboratory (NSF's NOIRLab) Tucson 85719, USA

[4]Communications, Education and Engagement, National Optical-Infrared Astronomy Research Laboratory (NSF's NOIRLab) Tucson 85719, USA

[*]To whom correspondence should be addressed; E-mail: kyba@gfz-potsdam.de.
[†]Current address: European Organization for the Exploitation of Meteorological Satellites (EUMETSAT), Darmstadt 64295, Germany.

The artificial glow of the night sky is a form of light pollution, and its global change over time is not well known. Developments in lighting technology complicate any measurement, due to changes in lighting practice and emission spectrum. We investigated the change in global sky brightness during 2011 to 2022 using 51,351 citizen scientist observations of naked eye stellar visibility. The number of visible stars has decreased, by an amount that can be explained by an increase in sky brightness by 7-10% per year in the human visible band.

This is faster than emissions changes indicated by satellite observations. We ascribe this difference to spectral changes in light emission, and to the average angle of light emissions.

Main Text

Over much of Earth's land surface, the night sky no longer fully transitions to starlight and moonlight after the sunset (*1*). Instead, the sky also glows with an artificial twilight, caused by the scatter of anthropogenic light in the atmosphere (*2*). The radiance of skyglow grew exponentially for much of the 20th century (*3*) due to population growth, the expansion of settlements, and deployment of new lighting technologies (*4, 5*). The character of the night is now changed from the conditions under which life evolved and civilization developed.

Many of the behavioral and physiological processes of life on Earth are connected to daily and seasonal cycles. For example, visual predation requires sufficient light to see, and predator-prey interactions are therefore expected to be affected by skyglow (*6*). There are few controlled field studies of the ecological impacts of skyglow, but it has been shown to impact plants, animals, and their interactions in the field (*7*), and laboratory studies have demonstrated changes in the physiology of fish at skyglow-like nighttime illuminance of 0.01 lux (*8*). In addition to its environmental consequences, skyglow limits human observation of starry skies and the Milky Way. Increasing skyglow has affected human culture (*9*), not only by restricting stargazing and astronomy, but also by changing the overall appearance of the night sky.

Effective methods for reducing light pollution are well understood (*10, 11*), and many of them also reduce electricity consumption. These measures have been implemented on local scales (*12, 13*), but have not seen widespread adoption. Nevertheless, awareness of light pollution led some policymakers to introduce measures that attempt to control light pollution (*14*).
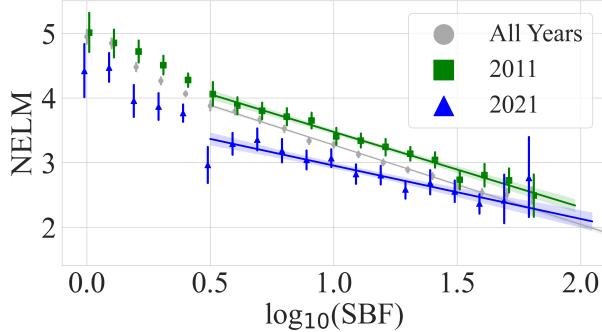
During the 2010s, many outdoor lights were replaced by light emitting diodes (LEDs):

global LED market share for new general lighting grew from under 1% in 2011 to 47% in 2019, and LED market share for new outdoor lighting in the United states was 66% in 2020 (*15*). The impact on skyglow from this transition to LEDs is unclear. There are some predictions that it will be beneficial (*16*), and others that it could be harmful due to spectral changes (*17*) or a rebound effect (*18*), in which the high luminous efficacy (more light emitted for a given power) of LEDs leads to more or brighter lights being installed, or longer hours of operation.

The generation of skyglow and changes in its character are related to social, economic, and technological processes, and skyglow trends therefore surely differ within and across countries. This means that time-series measurements of skyglow from individual sites, while important, may not be representative of how skyglow is changing on larger scales. It would therefore be beneficial if there were a way to measure how skyglow is changing on the continental and global scale.

It is in principle possible to directly measure skyglow via satellite observations of Earth at night (*19*). Unfortunately, the only existing satellite instrument that monitors the whole Earth has limited resolution and sensitivity, and is not able to detect light below 500 nm (*20*). This is a problem for three reasons: i) shorter wavelengths scatter more effectively in the atmosphere, increasing the chance that a photon emitted upward returns to Earth as skyglow (*2*). ii) LEDs marketed as white usually have an emission peak between 400-500 nm, where the satellite sensor is insensitive. iii) human visual sensitivity shifts towards shorter wavelengths at night (*11*). The first two effects could mean changes in ground radiance observed by satellite (*21, 22*) differ from changes in skyglow. The third effect means ground-based radiometers (and photometers) face a similar problem: if skyglow darkens at longer wavelengths but brightens at shorter wavelengths, it may be unclear whether the number of stars visible to humans would increase or decrease (*23, 24*).

We analyzed a citizen science dataset in which the human visual system was directly used

Figure 1: **Naked eye limiting magnitude estimated by Globe at Night participants as a function of the night sky brightness in 2014**. The sky brightness factor (SBF) is the ratio of total radiance to natural sky radiance, so SBF=1 means starlight and $\log_{10}$SBF=1 means the sky is 10 times brighter than starlight (*26*). The relationship is shown for 2011 (green squares), 2021 (blue triangles), and the average of all years from 2011-2022 (gray circles). Smaller NELM values mean fewer stars are visible. Lines indicate linear models fitted to the data for $\log_{10}$SBF>0.5, which corresponds to about 3 times brighter than starlight. Shaded regions show the 95% confidence interval.

as a sensor (*24, 25*). In the Globe at Night project (operated by NSF's NOIRLab), participants are presented with a set of star maps, and asked which one best matches the night sky at their location (see (*26*) and Fig. S1). This provides an estimate of the "naked eye limiting magnitude" (NELM, the magnitude of the faintest star that can be seen, which is smaller for brighter skies). This is related to skyglow, because as background radiance increases, faint point sources of light become invisible (*27*). The limiting magnitude estimated by citizen scientists using this method correlates with the locations of skyglow determined using satellite datasets (*24, 25*). We group different regions of the globe according to their World Atlas (*1*) sky brightness in 2014, in order to examine how the NELMs in these similarly bright areas change over time (Fig. 1, Fig. S2).
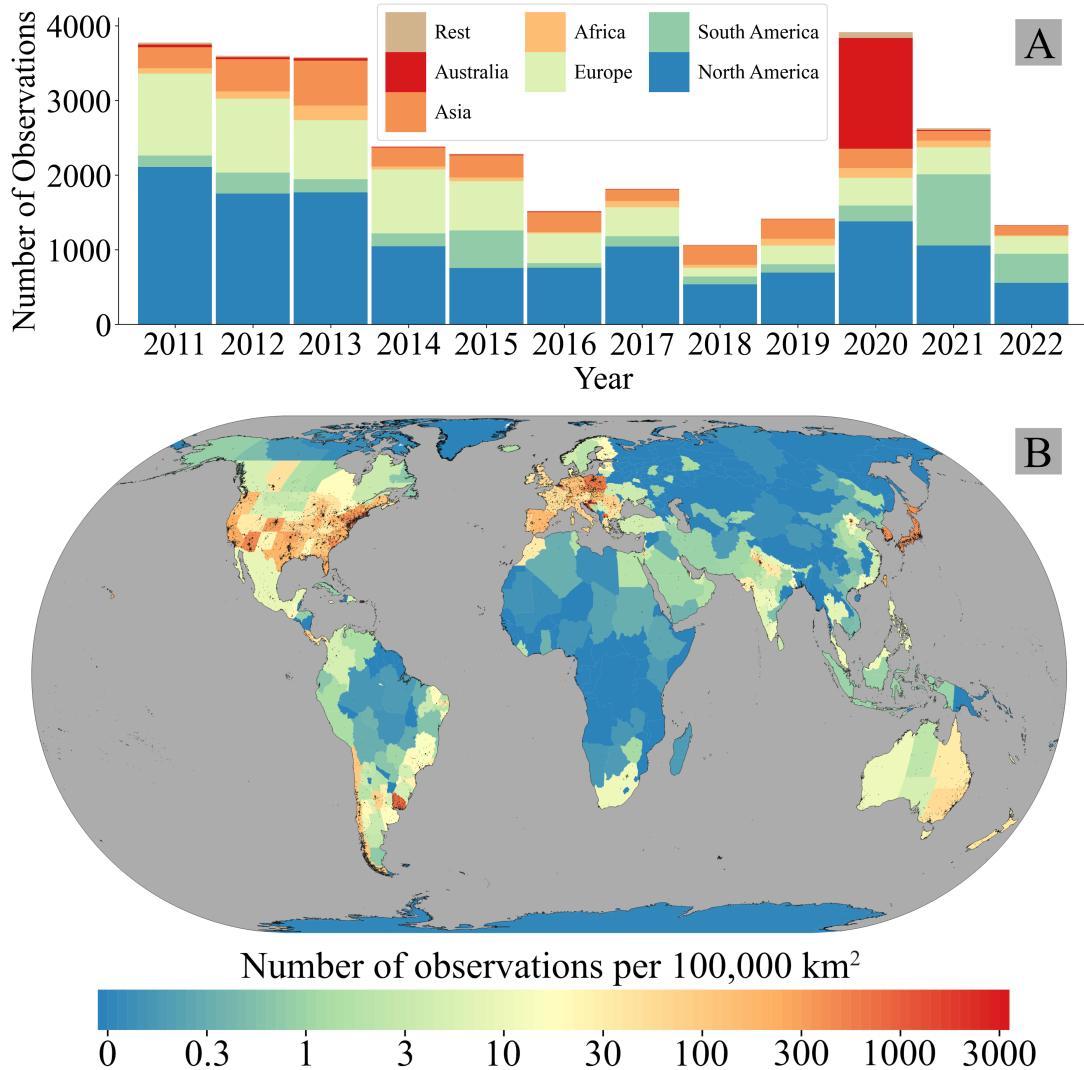
Our method accounts for differences in the set of citizen scientists participating each year (Fig. 2), and allows us to measure changes in stellar visibility on global or continental spatial scales. The overall number of observations limits the spatial and temporal scales over which trends can be determined (particularly for developing countries, where rapid skyglow change is

4

suspected but little observational evidence is available). The Globe at Night data has a spatial bias towards Europe, North America (especially USA), and a small number of other countries; there is also a bias towards inhabited areas. For example, 50.6% of the Asian contributions are from Japan, and contributions from Australia are overwhelmingly from coastal areas (Fig. 2B, S3) during 2020 (Fig. 2A). Because Europe and North America have sufficient data in both time and space, we report trends for those continents, and combine all the others (referred to as Rest of World hereafter).

While this dataset does not represent an average of either the land area or human population distribution, participants were concentrated in regions where skyglow is most prevalent (*1*). The global trend in skyglow we measure likely underestimates that in countries with the most rapid increases in economic development, because the rate of change in light emission is highest there (*21*) and we expect the addition of new lights to have a greater impact on skyglow than the replacement of existing lights.

To convert from the NELM measurements to rates of change in effective skyglow radiance for human vision, we fit a model to a subset of the dataset (observations from 2011 to August 2022, without twilight, moonlight, or a report of snow on the ground (*26*)) using a maximum likelihood method. There are five free parameters in the model: i) the average limiting magnitude reported in regions with no light pollution (y-intercept in Fig. 1), ii) the slope of the relationship between NELM and World Atlas skyglow radiance (similar to the slope in Fig. 1, but with a time-adjusted radiance), iii) the annual rate of change in artificial skyglow, iv) the standard deviation in the residuals between measured and predicted NELM, and v) an estimate of the error rate in the Globe at Night dataset (e.g. due to participants reporting their location or NELM incorrectly).

We find that the change in the number of visible stars reported by Globe at Night participants is equivalent to a 9.6% per year annual increase in sky brightness, averaged over the locations of

Figure 2: **Participation in Globe at Night during 2011 to August 2022**. (A) Bar chart showing the temporal distribution. Participation each year is subdivided by continent, as indicated in the legend. (B) Spatial distribution of all years combined. Colors indicate the participation normalized by land area. Black points show the locations of individual observations (these are emphasized in Fig. S3). Some of the largest countries have been divided into smaller jurisdictions. A logarithmic color scale and equal-area Eckert IV map projection are used.

6

participants (Table 1). For an 18 year period (such as the duration of a human childhood), this rate of change would produce more than a factor of four increase in sky brightness. A location with 250 visible stars would see that reduce to 100 visible stars over the same period. Because our method uses measurements made with human vision, it takes into account both the shift in spectrum and changes in sky radiance/luminance on human views of the night sky.

We confirmed this finding by performing an alternative analysis of the data. Instead of using a maximum likelihood method to fit a model of the skyglow change, we performed least squares fitting of a linear model to the monthly (observed minus expected) NELM residuals under the assumption that skyglow remains constant (Fig. 3A) or increases at a rate of 9.6% per year (Fig. 3B). The best fitting rate of change in NELM residuals is -0.044±0.007 magnitude per year for the uncorrected model, and 0.001±0.007 magnitude per year for the model corrected for skyglow increase. The even distribution of points above and below zero in the corrected model show that the trend is not being driven by outliers at the start or end of the analysis period (Fig. 3B).

The rate of skyglow increase we find is much larger than the rates of growth in light emissions observed by satellite in the 500-900 nm band: 2.2% per year globally during 2012-2016 (21) and >1.6% per year during 1992-2017 (with the possibility of faster increases in the visual band from 2012 onward) (22). For a more direct comparison, we analyzed the satellite radiance trends at the Globe at Night observation locations during 2014-2021 (26). Even after controlling for the locations, rates of change in upward radiance measured by satellite were also much smaller than our calculated rate of skyglow increase (Table S2). For example, for North America during 2011-2021, we find the rate of increase in skyglow radiance is 10.4±0.5%, compared to -0.8±0.04% in the surface radiance measured by satellite at these locations during 2014-2021 (Table S2). We ascribe the smaller satellite radiance change at Globe at Night locations compared to other studies (21, 22) to the tendency of Globe at Night participants to
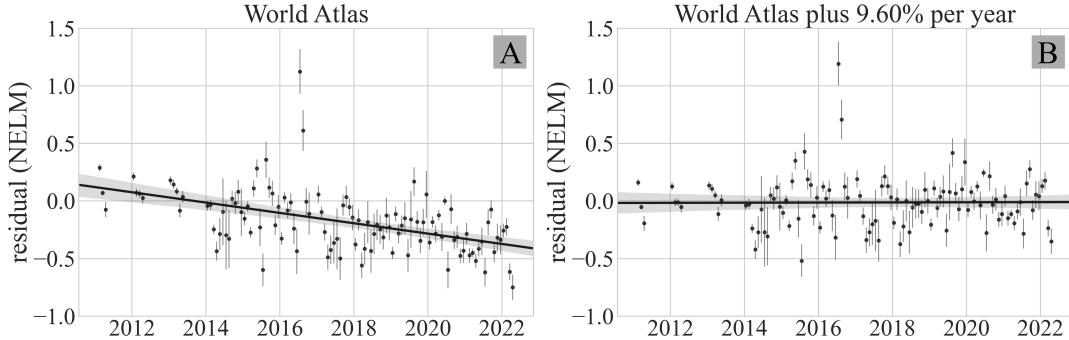
Region	$\hat{r}$	$\hat{N}_n$	$\hat{s}$	σ	E
	(%)	(NELM)		(NELM)	(%)
Europe	6.5 ± 1.0	4.77 ± 0.03	-1.33 ± 0.03	0.953 ± 0.012	2.4 ± 0.5
North America	10.4 ± 0.5	4.95 ± 0.02	-1.52 ± 0.02	1.009 ± 0.008	1.7 ± 0.3
Rest of World	7.7 ± 0.7	4.66 ± 0.03	-1.37 ± 0.02	1.077 ± 0.011	2.5 ± 0.5
Global average	9.6 ± 0.4	4.825 ± 0.014	-1.429 ± 0.014	1.022 ± 0.006	2.1 ± 0.2

Table 1: **Summary of results for different geographic areas**. Best-fitting values of our model are listed for three continental groupings, and the global average. $\hat{r}$ is the rate of increase, $\hat{N}_n$ the NELM for natural skies, $\hat{s}$ relates NELM to the World Atlas, σ is the standard deviation of residuals, and E is the error rate (*26*). Uncertainties are ±1 standard deviation, and are statistical only. Rest of World includes four continents due to insufficient coverage, see text. More detailed results, before combining continents, are listed in Table S1.

observe from residential areas (see Supplementary Text (*26*)).

These different results are not incompatible, because there are several differences between observing surface radiance with satellites and sky radiance as seen by humans on the ground. For example, the widespread conversion of streetlights from gas discharge lamps to LEDs (*16, 28*) could result in spectral changes which affect the two datasets differently, as discussed above. When cities maintain luminance after converting street lighting to LEDs, the spectral shift towards shorter wavelength (bluer) light causes the radiance observed by the satellite to decrease (*17*). In contrast, skyglow luminance after installation of LEDs could potentially either increase, due to increased atmospheric scattering of blue light (*2, 29*), or decrease, due to improved lighting fixtures that reduce horizontal emission (*16*).

The contribution to ground-observed skyglow and satellite-observed surface radiance depends on the lighting type. Most satellite radiometers have little to no sensitivity to light emitted towards the horizon (for example from a window or self-luminous sign) (*30*). However, light propagating towards the horizon is the largest contributor to skyglow, due to the order of magnitude longer path length from ground to space at such angles. In the early evening, a large fraction of the light that escapes cities is emitted by sources other than streetlights (*31*). Some of

Figure 3: **Difference from expected limiting magnitude under different skyglow growth models.** The monthly residuals (observed minus expected) for reported NELM relative to the expectation based on the World Atlas (Fig. 1) under two models. (A) The 2014 World Atlas with no growth. (B) The World Atlas radiance multiplied by an exponential increase of 9.6% per year relative to January, 2014 (*26*). Positive residuals mean observers reported more stars than expected. Error bars show the standard error, and data points before 2014 include higher numbers of observations than those afterwards. Black lines show a linear model fitted to the residuals, and the shaded region shows the 95% confidence interval of the fit.

these lighting applications, such as decorative and advertising lighting, produce a larger fraction of horizontally propagating light than modern street lighting. It is therefore likely that some of the differences between the rates of change for skyglow we calculate and those estimated from satellite data arise from changes in lighting practices or deployment.

We draw two conclusions from these results. First, the visibility of stars is deteriorating rapidly, despite (or perhaps due to) the introduction of LEDs in outdoor lighting applications. Existing lighting policies are not preventing increases in skyglow, at least on continental and global scales. Second, the use of naked eye observations by citizen scientists provides complementary information to the satellite datasets.

Supplementary materials: Materials and Methods, Figures S1-S3, Tables S1-S2, References (*34-37*).

References

1. F. Falchi, *et al.*, *Sci Adv* **2**, e1600377 (2016).

2. J. C. Barentine, *Nat Astro* **6**, 11201132 (2022).

3. F. Hölker, *et al.*, *Ecol Soc* **15**, (4) art 13 (2010).

4. K. Riegel, *Science* **179**, 1285 (1973).

5. J. Y. Tsao, P. Waide, *Leukos* **6**, 259 (2010).

6. C. C. M. Kyba, F. Hölker, *Landscape Ecol* **28**, 1637 (2013).

7. A. A. Wilson, *et al.*, *Integr Comp Biol* **61**, 1122 (2021).

8. F. Kupprat, F. Hölker, W. Kloas, *Environ Pollut* **262**, 114324 (2020).

9. T. Gallaway, *J Econ Issues* **44**, 71 (2010).

10. O. P. Cleaver, Control of coastal lighting in anti-submarine warfare, *Tech. rep.*, Engineer Board Fort Belvoir VA (1943). Report No. 746, GN 373. Access date: 2019 May 16.

11. F. Falchi, P. Cinzano, C. Elvidge, D. Keith, A. Haim, *J Environ Manage* **92**, 2714 (2011).

12. M. Aubé, J. Roby, *J Quant Spectrosc Radiat Transf* **139**, 52 (2014).

13. R. F. Green, C. B. Luginbuhl, R. J. Wainscoat, D. Duriscoe, *Astron Astrophys Rev* **30**, 1 (2022).

14. M. Morgan-Taylor, *Urban Lighting, Light Pollution and Society, Meier et al (eds)* (Routledge, 2015), chap. 9, pp. 159–176.

15. G. Zissis, P. Bertoldi, T. Serrenho, Update on the status of LED-lighting world market since 2018, *Tech. rep.* (2021). DOI:10.2760/759859.

16. B. Kinzey, *et al.*, An investigation of LED street lighting's impact on sky glow, *Tech. rep.*, US Department of Energy (2017). PNNL-26411.

17. L.-W. Hung, S. J. Anderson, A. Pipkin, K. Fristrup, *J Environ Manage* **292**, 112776 (2021).

18. J. Y. Tsao, H. D. Saunders, J. R. Creighton, M. E. Coltrin, J. A. Simmons, *J Phys D Appl Phys* **43**, 354001 (2010).

19. A. S. de Miguel, C. C. M. Kyba, J. Zamorano, J. Gallego, K. J. Gaston, *Sci Rep* **10**, 7829 (2020).

20. S. D. Miller, *et al.*, *Remote Sens* **5**, 6717 (2013).

21. C. C. Kyba, *et al.*, *Sci Adv* **3**, e1701528 (2017).

22. A. Sánchez de Miguel, J. Bennie, E. Rosenfeld, S. Dzurjak, K. J. Gaston, *Remote Sens* **13**, 3311 (2021).

23. A. Sánchez de Miguel, *et al.*, *Mon Not R Astron Soc* **467**, 2966 (2017).

24. C. C. Kyba, *Nat Astro* **2**, 267 (2018).

25. C. C. M. Kyba, *et al.*, *Sci Rep* **3**, 1835 (2013).

26. Materials and methods are available as supplementary material.

27. A. Crumey, *Mon Not R Astron Soc* **442**, 2600 (2014).

28. N. Schulte-Römer, J. Meier, M. Söding, E. Dannemann, *Sustainability* **11**, 6160 (2019).

29. C. B. Luginbuhl, P. A. Boley, D. R. Davis, *J Quant Spectrosc Radiat Transf* **139**, 21 (2014).

30. C. C. Kyba, *et al.*, *J Geophys Res-Atmos* **127**, e2021JD036382 (2022).

31. J. C. Barentine, *et al.*, *J Quant Spectrosc Radiat Transf* **253**, 107120 (2020).

32. C. Kyba, Y. O. Altıntaş, C. Walker, M. Newhouse, Software for analyzing Globe at Night data, GFZ Data Services DOI 10.5880/GFZ.1.4.2022.008.

33. F. Falchi, *et al.*, Supplement to: The new world atlas of artificial night sky brightness. GFZ Data Services., DOI `http://doi.org/10.5880/GFZ.1.4.2016.001` (2016).

34. Globe at Night webapp, URL `www.globeatnight.org/webapp`.

35. Scistarter Globe at Night page, URL `https://scistarter.org/globe-at-night`.

36. C. D. Elvidge, M. Zhizhin, T. Ghosh, F.-C. Hsu, J. Taneja, *Remote Sens* **13**, 922 (2021).

37. J. Coesfeld, T. Kuester, H. U. Kuechly, C. Kyba, *Sensors* **20**, 3287 (2020).

Acknowledgments

Funding

Author contributions

CK developed the analysis methodology, wrote some of the software, and wrote the initial draft of the article. YOA wrote the rest of the software and produced the images. CW initiated and manages the Globe at Night project. MN manages the Globe at Night database. All authors contributed to writing and editing.

Competing interests

CW is a director of the International Dark-Sky Association, and CK is a former director of the same body. We declare there are no other competing interests.

Data and materials availability

The Globe at Night web application is at `http://www.globeatnight.org/webapp/`, and data are available at: `https://www.globeatnight.org/maps.php`. The subset of the dataset we used, and our analysis code are archived at Deutsches GeoForschungsZentrum Potsdam (GFZ) Data Services (*32*). We also used the World Atlas data (*33*).

Science

AAAS

Supplementary materials for:

Citizen scientists report global rapid reductions in the visibility of stars from 2011 to 2022

Christopher C.M. Kyba, Yiğit Öner Altıntaş, Constance E. Walker, Mark Newhouse

Correspondence to: kyba@gfz-potsdam.de

This PDF file includes:

Materials and Methods

Figs. S1 to S3

Tables S1 to S2

Materials and Methods

Globe at Night methodology

Globe at Night participants submit data via a web application (*34*) either via a desktop or smartphone. The application consists of six data entry steps. First, the observers report the date and time that they made the observations. Second, the observers report their location, either by manually entering in a latitude and longitude, or else by clicking on a map. They then have the option of filling in additional comments about the location in a free text box. Third, observers select which one of eight star maps best matches what they see in the sky (Fig. S1). These maps show star fields for integer steps of naked eye limiting magnitude (NELM). Fourth, the observers report what the sky conditions were that night, first by choosing from one of four levels of cloudiness, and then by filling in an optional free text box. Fifth, observers have the option of also reporting the sky radiance measured with a Sky Quality Meter (SQM). Finally, observers have the option of entering their email address, to log their observation with SciStarter (*35*).

While Globe at Night has existed since 2006, the original campaigns were based on a printed paper form, rather than the webapp. This change could result in a systematic difference in NELM determination. For example, the webapp takes latitude into account in the display of which stars can be seen, rather than presenting the same maps for all participants worldwide. A second difference is that the participants view the stars on a backlit screen rather than via reflected light from a paper. We therefore decided to analyze only data taken using the webapp (from January 2011 to 16 August 2022). Before 2014, Globe at Night participation was restricted to one or more campaigns early in the year. From 2014 onward, participation in every month was possible (using different star fields). February and March have continued to be the most popular months for observations.

The participation in Globe at Night decreased in the later part of the 2010s (Fig. 2A). If

the types of people participating changed over time, this could introduce a systematic bias in the estimation of NELM. For example, people with greater observing experience are able to see more stars, and as people age they are able to see fewer stars (*27*). If the Globe at Night participant pool was fixed and never changed, one might therefore expect that fewer stars would be seen over time as the participants aged. We therefore organized a special campaign in February and March of 2020, to boost participation and change the mix of participants. If an expansion in participation following media attention were to be connected with a reverse in the trend in the data, that would suggest that the observed trend is affected by changes in who is participating. We do not observe such an effect: the trend of decreasing NELM continued into the 2020s (Fig. 3A).

The web application for Globe at Night and "activity guides" are available in multiple languages. In 2011, the webapp was available in English and Spanish, and activity guides were available in 16 languages. In 2022, these were 28 and 21 languages respectivly. However, the webapp was mostly used in English, even in countries where the webapp is available in the national language.

If lighting were to change in a way such that more direct light shone towards the participants (i.e. became more glaring), this could make it more difficult to observe stars. It is conceivable that conversion from orange sodium vapor streetlights to white LEDs in residential areas could play some role. However, regardless of whether a change in glare (rather than increased sky-glow) could explain some of the shift, this also reduces the number of stars visible to humans.

Data selection

Before we analyzed the data, several steps were taken to ensure a consistent dataset. When a data record is submitted, Globe at Night employs a set of automated checks before accepting the observation into their database. For example, spammers sometimes post html links in free-text

fields, so reports containing links or email addresses are automatically removed. Latitude and longitude are also compared to a country boundary database. In the case they do not match, then the data record is not included. If these tests are passed, the data is added to the public online database. The rest of the data selection steps described below take place after this automated step.

We include only observations for which the observer reported no clouds in the sky. We check the optional free-text fields in the data report to look for the word "snow" (in English, French, German, Italian, and Spanish). These reports are rejected, unless they satisfy a simple check indicating that the participant was likely reporting that there was "no snow" (e.g. "pas de neige" in French). This check removed 1,755 observations. We calculate the position of the Sun and Moon for the observer's location at the Coordinated Universal Time (UTC) of the observation, and reject observations for which twilight is present (solar elevation angle $> -18°$) or the Moon is above the horizon (lunar elevation angle $> 0°$). We also reject observations for which an SQM observation was submitted, because Globe at Night allows observers to submit SQM observations without submitting a visual observation, and in this case the system generates and stores an approximate NELM value in the database based on the radiance. Because the public database does not record whether the NELM was generated automatically, for the sake of reproducability we reject all observations that include an SQM report. Together, these steps reduced the dataset from 83,989 cloud-free observations to 51,351 usable observations during the period January 2011 to August 2022.

Next, we apply geographic and temporal binning, to deal with situations where a certain location has multiple observations. This can happen, for example, when a single person makes multiple observations within the same month, or when a group of people make an observation at the same time and place. We bin the observations geographically according to the 30 arcsecond grid of the World Atlas of Artificial Night Sky Brightness (1), and find the monthly mean

4

of all NELM observations for each grid square. This reduced the dataset to 29,316 monthly observations, and each of these are treated as having equal weight. The observation numbers in Fig. 2 and Table S2 consist of the data after each of the selection processes above have been completed.

World Atlas

Volunteered geographic information is not necessarily collected in a systematic way. In the case of Globe at Night, the areas in which participants are active changes from year to year, sometimes quite dramatically (e.g. Australia in 2020 thanks to an organized event, and Uruguay in 2021, Fig. 2A). We address this by comparing sky brightness reported by Globe at Night participants to a world map of artificial sky brightness (1), which was based on satellite data (20, 36) from 2014. With this approach, we can bin observation locations according to their predicted 2014 sky brightness (Fig. 1 and Fig. S2), and also predict how bright the sky was at different times, based on modeled lighting changes (as below). Because the World Atlas only extends from 60° South to 75° North, the dataset is reduced from 29,316 to 29,313 observations.

Maximum likelihood fit

We use a maximum likelihood method to estimate the global rate of change in sky brightness, based on the assumption that the artificial component of sky brightness is increasing (or decreasing) exponentially:

$$B = B_0 + A(1 + \hat{r})^t \tag{S1}$$

where B is our predicted sky brightness for any given location at time t, B_0 is the average brightness of a natural night sky (fixed at $0.174 \, \text{mcd} \, \text{m}^{-2}$, the value used by the World Atlas), A is the artificial component of sky brightness for 2014 according to the World Atlas, and $\hat{r}$ is the fractional increase or decrease per year (a free parameter). We define t as the date after the

5

beginning of 2014:

$$t = y - 2014 + (m - 0.5)/12 \qquad (S2)$$

where y is the year and m is the month.

For any predicted sky brightness B, the expected naked eye limiting magnitude ($\hat{N}_e$) for the average globe at night observer is assumed to be given by:

$$\hat{N}_e = \hat{N}_n + \hat{s} \log_{10} \frac{B}{B_o} \qquad (S3)$$

Here $\hat{N}_n$ (the NELM reported under natural skies) and $\hat{s}$ (a factor which relates NELM to the logarithm of the World Atlas brightness) are free parameters, and the ratio B/B_o is the predicted brightness of the sky relative to the natural starlit sky. Note that this is a linear equation, where $\hat{N}_n$ is the y-intercept, and $\hat{s}$ is the slope. Two examples of this function are shown in Fig. 1. When the artificial component of sky brightness is zero, then $\hat{N}_e = \hat{N}_n$ regardless of the rate of growth or the year. This means that if the model is valid, then the average reported NELM in areas with no artificial light should remain stable from year to year.

Given an expected NELM $\hat{N}_e$, we estimate the probability that an observer would report any particular NELM N. In Globe at Night, the star maps are fixed to integer values of NELM, so we cannot use a continuous distribution to model these probabilities. Instead, we assume that the probability distribution can be approximated by integrating a Gaussian distribution between ± 0.5 NELM. Observers are not allowed to report NELM outside of range 0 to 7, so for the case of N=0 or N=7 we integrate the distribution to positive and negative infinity. Given that Globe at Night observers sometimes either report erroneous NELM values or make an error in reporting their position, we also assign an equal error probability ($E/8$) to each NELM bin, where E is the total error rate. For any given observation, the probability of observing a NELM

N given a particular expected NELM of $\hat{N}_e$ is therefore:

$$P(N|B_0, r, N_n, s, \sigma, E) = P(N|\hat{N}_e, \sigma, E) = (1 - E) \int_{N-0.5}^{N+0.5} \frac{1}{\sigma\sqrt{2\pi}} e^{-\frac{1}{2}(\frac{N-\hat{N}_e}{\sigma})^2} dN + E/8$$

(S4)

where σ is the (fit) standard deviation of differences relative to $\hat{N}_e$, and E is the error rate (both are free parameters). The variable σ provides an indication of the precision of the method (25).

In the case of erroneous (or faked) data, the term in the integral will generally be small, because N is unlikely to be close to $\hat{N}_e$ by chance alone. This means that the probability will stay near $E/8$ regardless of the free parameters, and the observation will therefore contribute little information to the determination of the maximum likelihood. The low fit values of E in the different regional analyses are 2-3% (Table S1), indicating that the vast majority of the submitted observations report plausible NELM values.

The likelihood function $\mathcal{L}$ for the Globe at Night dataset is:

$$\mathcal{L} = \prod P(N_o|B_0, r, N_n, s, \sigma, E)$$

(S5)

where B_0, r, N_n, s, σ, and E are free parameters. When this function is maximized (in practice, by minimizing the negative log likelihood), the best fitting parameters are obtained. The uncertainty on each parameter is the square root of the diagonal terms of the inverse of the Hessian matrix, evaluated at the best fitting values. We verified that the uncertainties had nearly identical sizes in both positive and negative directions (by varying the variables individually and evaluating when the negative log likelihood increased by 0.5), and therefore report 1 standard deviation uncertainties on the mean.

In addition to evaluating the Globe at Night dataset as a whole, we also divided the world into three regions (North America, Europe, and Rest of World), and ran the minimization separately for each of them. This division reflects the rough breakdown of the submitted Globe at Night data (Fig. 2), which has more participation in wealthier countries. The total num-

bers of observations are 13,456 for North America, 6,529 for Europe, and 9,328 for Rest of World. For both Europe and North America (particularly the United States), observations are distributed across many countries (and states), so we consider these results representative of the continental averages. In contrast, our results for the other four continents (Table S1) cannot be considered representative of the whole continents, because of either poor spatial coverage (Africa, Asia, South Africa) or poor temporal coverage (Australia), as shown in Fig. 2.

Satellite radiance analysis

For comparison with satellite data (*20*), we analyzed radiance from the Visible Infrared Imaging Radiometer Suite Day-Night Band (DNB) at the individual locations at which Globe at Night observations were reported. As a first step, we listed the Globe at Night observing locations (on the 30 arcsecond grid of the World Atlas). There were 22,076 of these positions (compared to 29,316 monthly data points used in the main analysis). For each of these locations, we then determined the radiance calibrated DNB observations from the Earth Observation Group's annual time series (*36*), corrected for variations in atmospheric airglow (*37*). We do not include DNB data from 2013 because the airglow correction is not available for the annual composite of that year. We chose the Earth Observation Group's (EOG) composites rather than NASA's Black Marble composites for two reasons. First, the airglow correction is currently only available for EOG data. Second, the Black Marble minimum radiance cut can introduce difficulties for time series analyses in regions that are faintly lit, because radiances frequently jump between zero and values just above the cut, rather than being continuously distributed.

We next fitted a linear model to each of the time series, calculating for each location the slope m_u and y-intercept b_u. We used a linear rather than exponential fit because areas with little artificial light emission often have negative radiance after the airglow correction. In order to compare to the exponential rates of change from the Globe at Night analysis, we therefore
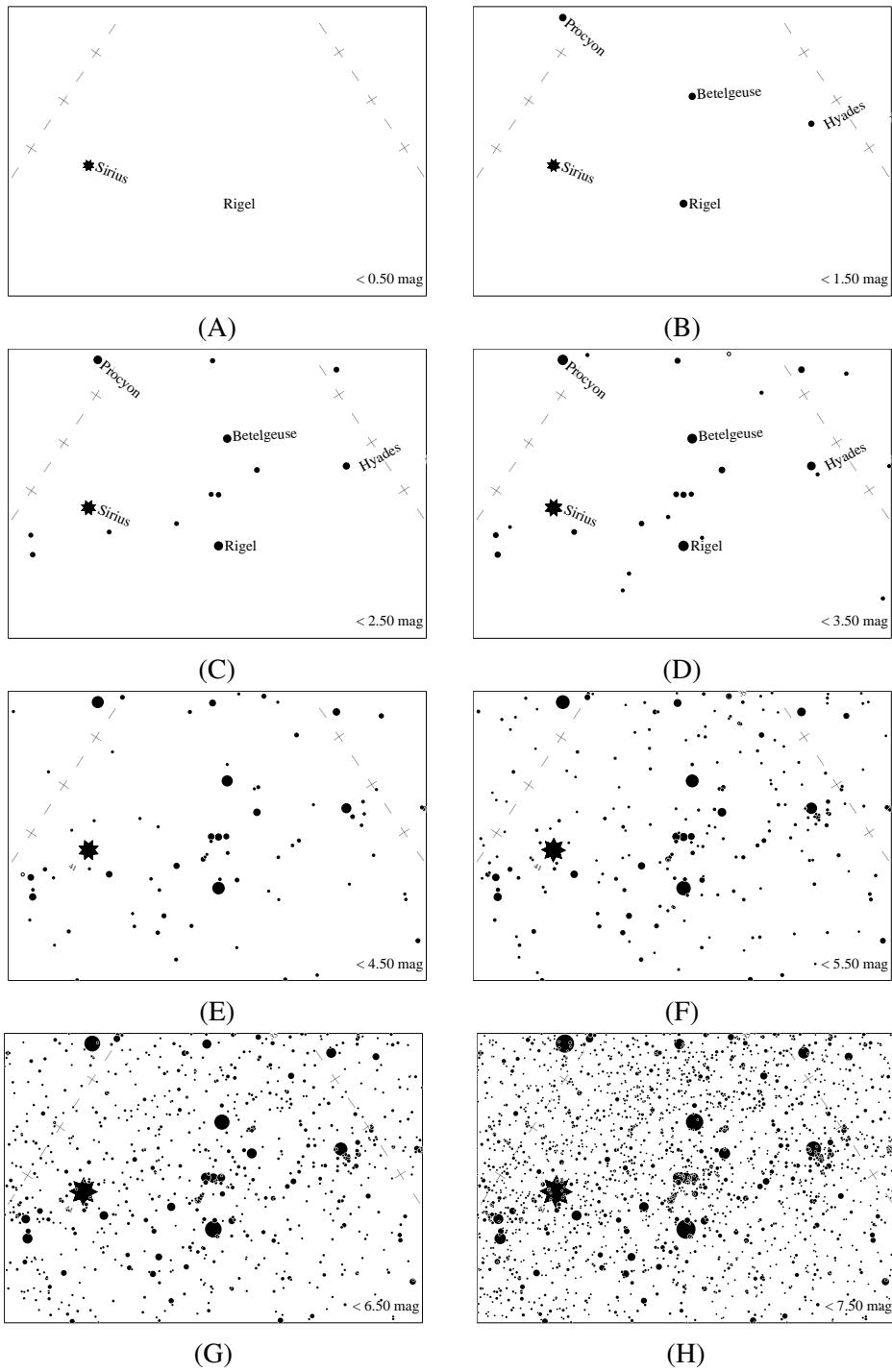
8

approximated the annual percentage rate of change (r) based on the slope relative to the fit radiance at the halfway point:

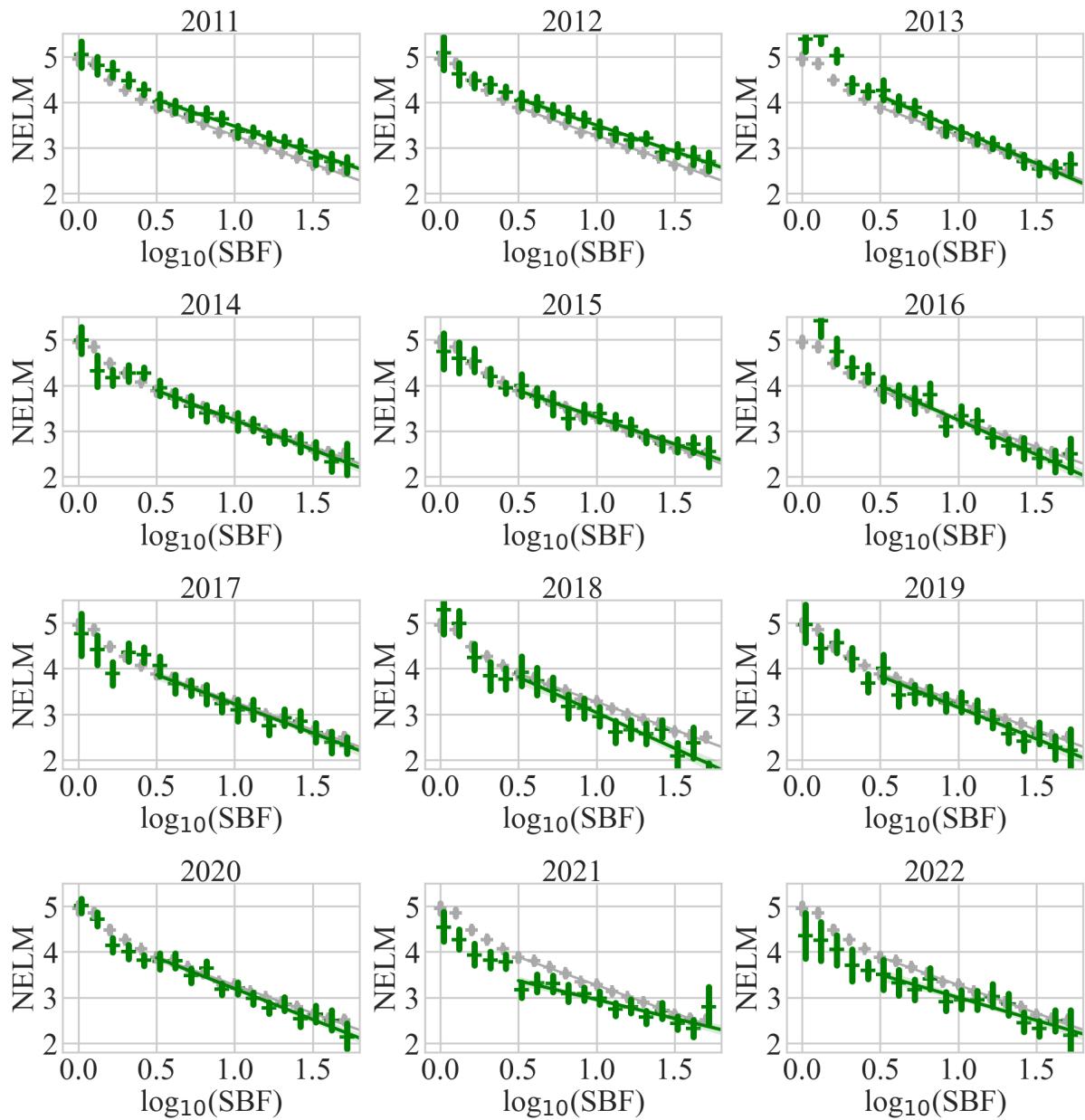$$r \approx \frac{m_{\mathrm{u}}}{2017.5 \cdot m_{\mathrm{u}} + b_{\mathrm{u}}} \cdot 100\% \qquad \text{(S6)}$$

Time series that had an estimated 2017 radiance value below 0.5 nWcm^{-2}sr^{-1} were removed from the analysis, because such regions are generally unlit, and the time series therefore consists mainly of noise.

Finally, we computed the the median, mean, and standard error of the set of trends in each of the different analysis regions (Table S2). The trend distribution has non-Gaussian tails, which we ascribe to changes in development. (Consider, for example, the case of a hypothetical observation submitted in 2020 from a residential subdivision that did not exist until 2017. The radiance would increase greatly from the small base that existed on the undeveloped land before construction started, and the linear regression would therefore return a very large annual growth rate.) Regardless, the details of the shape of the distribution do not affect our conclusions, because the mean and median trends in DNB radiance are all far smaller than the rate of skyglow growth inferred from the Globe at Night data for all regions (Table S2).
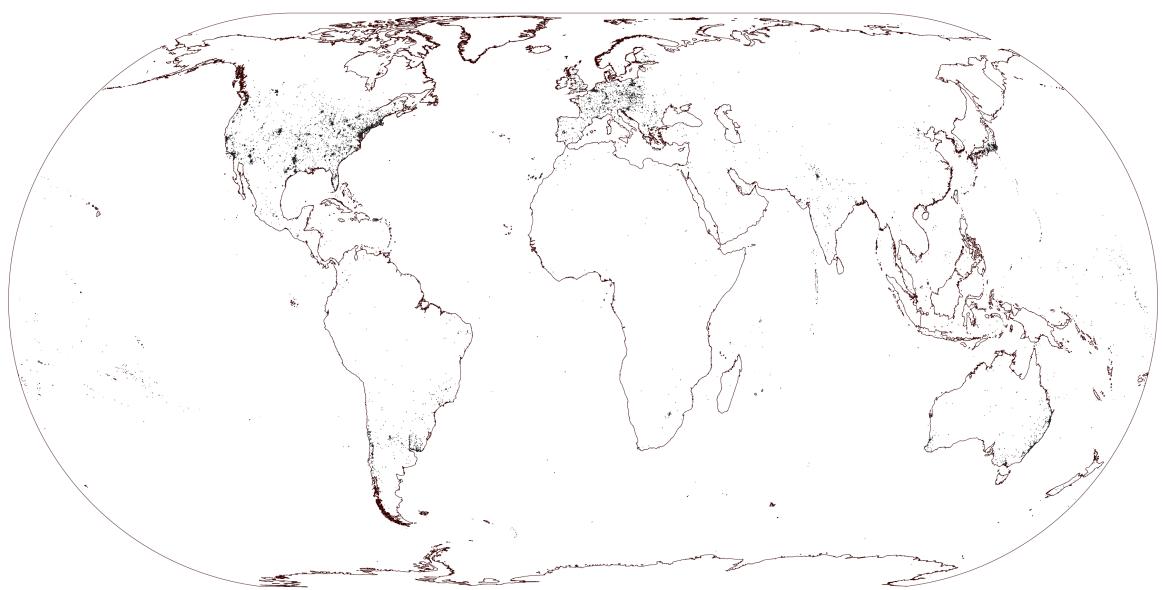
In this analysis, all locations are weighted equally and changes are relative. An increase of 0.1 nWcm^{-2}sr^{-1} in a region that had on average 10 nWcm^{-2}sr^{-1} is therefore treated the same as an increase of 1 nWcm^{-2}sr^{-1} at a location with an average radiance of 100 nWcm^{-2}sr^{-1}. These rates of change are not representative for the continents as a whole. They only consider areas in which Globe at Night participants submitted observations, and are therefore likely biased towards residential areas. Other areas such as commercial city centers, greenhouses, and industrial areas contribute to area-averaged upward directed radiance (*21,22*), but are less likely to be selected as Globe at Night observation sites.

Figure S1: **Example star charts used by Globe at Night.** Eight constellation maps from the Globe at Night webapp for a latitude of 30° North are shown for the Orion constellation with naked eye limiting magnitudes in integer steps of 1 from 0 (A) to 7 (H).

Figure S2: **Same as Figure 1, but for every year separately**. Green points and lines are the measurements in each individual year, gray lines are the average of all data from 2011-22.

Figure S3: **Locations of Globe at Night observations during 2011 to August 2022.** Black points show the locations of individual observations, as in Fig. 2, but with the country boundaries and colors removed to emphasize the positions of the observations.

Region	Number of observations	$\hat{r}$ (%)	$\hat{N}_n$ (NELM)	$\hat{s}$	σ (NELM)	E (%)
Africa*	919	27 ± 4	4.40 ± 0.08	-1.15 ± 0.09	1.04 ± 0.04	3.1 ± 1.9
Asia*	3,317	5.8 ± 0.9	4.65 ± 0.05	-1.61 ± 0.04	0.93 ± 0.015	2.5 ± 0.6
Australia†	1,642	18 ± 4	5.19 ± 0.07	-1.27 ± 0.08	1.09 ± 0.03	3.3 ± 1.3
Europe	6,529	6.5 ± 1.0	4.77 ± 0.03	-1.33 ± 0.03	0.953 ± 0.012	2.4 ± 0.5
North America	13,456	10.4 ± 0.5	4.95 ± 0.02	-1.52 ± 0.02	1.009 ± 0.008	1.7 ± 0.3
South America*	3,257	29 ± 2	4.51 ± 0.05	-0.88 ± 0.04	1.040 ± 0.018	3.1 ± 0.8
Global average	29,313	9.6 ± 0.4	4.825 ± 0.014	-1.429 ± 0.014	1.022 ± 0.006	2.1 ± 0.2

Table S1: **Same as for Table 1, but for all continents separately**. Outside of Europe and North America, the results should not be considered representative because of either poor spatial (*) or temporal (†) coverage. The "overall" values include a small number of observations that do not fit within the continental boundaries we used.

Region	Number of locations	Median Radiance (nWcm^{-2}sr^{-1})	Mean Rate of change (%)	Median rate of change (%)
Africa	452	17 [2.0, 60]	0.0 ± 0.3	0.0
Asia	2,280	24 [4.0, 50]	0.85 ± 0.09	0.73
Australia	1,332	7.3 [1.9, 20]	0.02 ± 0.12	-0.22
Europe	3,699	8.4 [1.3, 35]	-0.32 ± 0.09	-0.19
North America	9,488	14 [2.4, 37]	-0.80 ± 0.04	-0.95
South America	1,995	33 [6.3, 64]	1.24 ± 0.12	0.71
Global average	19,262	14 [2.2, 43]	-0.23 ± 0.03	-0.37

Table S2: **Summary of Day Night Band radiance trends at Globe at Night observation sites for different geographic areas**. The 68.3 percentile range is shown with the radiance rather than a standard deviation, because the distribution is non-Gaussian. Uncertainties on the mean rate of change are are ± 1 standard deviation and represent the standard error. The global average values include a small number of observations that do not fit within the continental boundary map we used.